Modelling of embayed beach equilibrium planform and rotation signal

Bruno Castelle, Arthur Robinet, Déborah Idier, Maurizio d'Anna

Modelling of embayed beach equilibrium planform and rotation signal

Bruno Castelle[1], Arthur Robinet[2], Déborah Idier[3], Maurizio D'Anna[1,3]

[1]UMR CNRS EPOC, Université de Bordeaux, France

[2]BRGM (French Geological Survey), Pessac, France.

[3]BRGM (French Geological Survey), Orléans, France.

Corresponding author: bruno.castelle@u-bordeaux.fr

Abstract

Embayed beaches are highly attractive sandy beaches bounded laterally by rigid boundaries, which deeply affect equilibrium beach planform and shoreline dynamics. We use LX-Shore, a state-of-the-art shoreline change model coupled with a spectral wave model to address embayed beach shoreline dynamics driven by longshore sediment transport processes. The model is applied to different idealized embayed beach configurations including variations in headland lengths. The model simulates a large range of equilibrium embayed beach planforms and associated spatial and temporal modes of shoreline variability. For short headlands enabling occasional headland sand bypassing, both embayed beach curvature and maximum erosion at the upwave side of the embayment increases with increasing headland length. Beach curvature also increases with increasing headland length for headlands long enough to prevent any headland sand bypassing. In contrast, at the same time, embayed beach becomes increasingly curved and symmetric, with maximum localised erosion within the embayment decreasing in intensity. When there is no headland sand bypassing, rotation signal decreases in amplitude and becomes increasingly symmetric with increasing headland length. The modal (time-invariant) directional spreading of incident waves is critical to embayed beach behaviour, with the envelope and variance of cross-shore shoreline change and time-averaged shoreline curvature all increasing with decreasing modal directional spreading. Embayed beach rotation characteristic timescale increases with increasing embayed beach length, while the narrower the embayment the smaller the cross-shore amplitude of shoreline variability. Our simulations provide new insight into the influence of embayment characteristics and incident wave conditions on equilibrium planform and shoreline dynamics of embayed beaches. This work also implies that the degree of potential headland sand bypassing should be taken into account for modelling of beach rotational dynamics and embayed beach dynamic planform configuration.

Highlights

- Embayed beach shoreline response is simulated with a hybrid shoreline model
- Headland length and headland sediment bypassing control shoreline response
- Wave directional spreading is critical to both mean shoreline and rotation signal
- Embayment beach length controls rotation characteristic timescale

Keywords: embayed beach ; hybrid shoreline model ; headland length ; rotation ; equilibrium beach planform; headland sand bypassing

1. Introduction

Embayed beaches are sandy beaches bounded laterally and vertically by rigid boundaries (Loureiro et al., 2012a), which can deeply affect incident wave conditions and, in turn, breaking wave conditions (e.g., Daly et al., 2014a), beach morphodynamics (e.g., Castelle et al., 2012; Blossier et al., 2016; McCarroll et al., 2016) and shoreline variability (e.g. Ranasinghe et al., 2004; Ojeda and Guillen, 2008; Turki et al., 2013a; Harley et al., 2015; Robinet et al., 2020a). These physical boundaries include artificial coastal defences like groins, harbour walls and breakwater, and natural rocky headlands and submerged rocky platforms. Artificial coasts (e.g., approximately 30% of the French coastline, CEREMA, 2017) and hilly/mountainous coasts (Short and Masselink, 1999) constitute a large proportion of the world's coastlines, making embayed beaches ubiquitous globally. Due to the large natural variability of wave exposure and headland characteristics (Fellowes et al., 2019), embayed beaches exhibit a striking planform variability (Figure 1). Therefore, understanding and modelling embayed beach dynamics is an important but complex research area.

Over the last decades, a lot of attention has been paid to describing the time-averaged, equilibrium planform of embayed beaches (e.g., Yasso, 1965; Sivester, 1970; Rea and Komar, 1975). The equilibrium beach concept was used to derive a number of static equilibrium models (Hsu et al., 1987; Hsu and Evans, 1989), which are generally based on a single representative wave direction, a down-coast control point and a diffraction point. Parabolic bay shaped models (Hsu and Evans, 1989) were preferred to log-spiral models (Yasso, 1965; Sivester, 1970), and became the most widely used approach to understanding the stability of embayed beaches (Hsu et al., 2004; Jackson and Cooper, 2010, Hsu et al., 2010). These equilibrium shoreline planform models, however, do not always show good skill (Gonzalez and Medina, 2001; Klein et al., 2003a,b), for example near estuary mouths or where there is a strong geological control of beach morphology (e.g., intertidal to subtidal rocky

platform, Jackson and Cooper, 2010). Even when general settings are favourable to such model application, there are still limitations. For instance, a strong underlying assumption is that swell waves arrive persistently from a narrow range of directions, which is challenged on many coasts with multimodal wave climates. Such models also assume that alongshore wave height gradient is controlled by one diffraction point, while on natural coasts many diffraction points can co-exist and can even migrate across rocky platforms as the tide fluctuates (Jackson and Cooper, 2010). In addition, as noted by Daly et al. (2014a) diffraction is dominant only for strongly curved embayments when wave conditions are narrow-banded. Otherwise, refraction typically overwhelms diffraction effects. In addition, these models do not take into account headland sediment bypassing, which can have a profound impact on equilibrium shoreline planform as suggested by Goodwin et al. (2013). To overcome these issues and to address a wider spectrum of natural embayed beaches, equilibrium shoreline models are still under development (Elshinnawy et al., 2018a,b,c).

The processes governing the morphodynamics of embayed beaches on the timescales from storms to years/decades have been studied for decades (e.g., Klein et al., 2002; Ojeda and Guillen, 2008). Day by day wave forcing is the primary driver of alongshore and cross-shore sediment transport, leading to complex patterns of erosion and accretion along the embayment. Clockwise/counterclockwise rotation of the embayed beach planform has been commonly observed as the dominant pattern of shoreline variability at embayed beaches (Masselink and Pattiaratchi, 2001; Short and Trembanis, 2004; Ranasinghe et al., 2004; Martins and de Mahiques, 2006; Thomas et al., 2011; Loureiro et al., 2012a; Turki et al., 2013a; Van de Lageweg et al., 2013; Harley et al., 2013; Robinet et al., 2020a). Loureiro and Ferreira (2020) reviewed the mechanisms and timescales of beach rotation at embayed beaches. Beach rotation has long been attributed to longshore transport processes, when enough sediment moves from one side of the embayment to the other to shift the mean orientation of the beach (Ratliff and Murray, 2014). However, storms and variations in incident wave energy cause cross-shore sediment exchange and drive shoreline changes typically by tens of metres (Yates et al., 2009; Splinter et al., 2014). Harley et al. (2011, 2015) suggested a more complex conceptual model of beach rotation process at Narrabeen-Collaroy embayment (SE Australia) based on the analysis of an extensive dataset. They revealed that headland sheltering of oblique waves results in alongshore non-uniform wave exposure and cross-shore processes that, in turn, contribute significantly to observed beach rotation. Harley et al. (2015) therefore suggested that beach rotation occurs due to the complementary and interacting cross-shore and longshore processes at different timescales. Robinet et al. (2020a) used a state-of-the-art shoreline change model and demonstrated at the same coastal embayment that cross-shore processes drive a slightly alongshore variable cross-shore migration signal

on the timescales from hours (storms) to months, while longshore processes primarily contribute to rotation on longer timescales of months to seasons at this coastal embayment.

In recent years, a new generation of shoreline change models have been developed, offering the opportunity to simulate shoreline evolution at wave-dominated sandy beaches on the timescales from hours (storm) to years and decades with reasonable skill (Montaño et al., 2020). Process-based models, which are computationally expensive, require accurate selection and sequencing of representative wave conditions to address embayed beach dynamics (Daly et al., 2014b). Instead, the so-called "hybrid" models are based on general principles (e.g., Yates et al., 2009; Davidson et al., 2013; Vitousek et al., 2017; Robinet et al., 2018; Antolínez et al., 2019; Tran and Barthelemy, 2020) rather than on the detailed description of nearshore hydrodynamics, sediment transport and morphological changes through conservation of mass and momentum. Hybrid models can therefore simulate shoreline change with low computational cost. Along coastlines that are longshore transport dominated with presence of rigid physical boundaries such as headlands, one-line models have emerged as a powerful tool (e.g., Hanson, 1989; Larson et al., 2002; Szmytkiewicz et al., 2000; Ratliff and Murray, 2014; Hurst et al., 2015). All these models are essentially based on gradients in longshore sediment transport due to the alongshore variability in breaking wave conditions, but they vary in terms of numerical implementation and level of description on wave field transformation. Ratliff and Murray (2014) identified two primary orthogonal modes of shoreline behaviour around the mean that are the well-known rotation mode and a newly identified breathing mode, which represents changes in shoreline curvature. Hurst et al. (2015) examined the behaviour of embayed beaches forced by different directional wave climates. They showed that embayed beach planform curvature decreases with the spread of wave directions. However, in both studies headland sediment bypassing and the influence of headland length was not addressed. In addition, wave transformation was based on simple rules for the diffraction and refraction of waves where the coast was shadowed from incoming waves.

In this paper we use the state-of-the-art shoreline change model LX-Shore, which accounts for the detailed wave transformation to provide enhanced insight into embayed beach shoreline dynamics. LX-Shore model (Robinet et al., 2018) can simulate both the equilibrium embayed beach planform and a large range of spatial and temporal modes of shoreline variability even in complex natural embayed beaches, even with prominent rocky headland and submerged outcrops deeply affecting the incident wave field (Robinet et al., 2020a). The model is applied to different embayed beach configurations. We systematically address the influence of headland length on equilibrium embayed beach planform and shoreline dynamics on the timescales from hours to decades.

2. Method

2.1. *LX-Shore model*

LX-Shore is a two-dimensional planview cellular-based one-line shoreline change model for wave-dominated sandy coasts developed by Robinet et al. (2018), with additional process implementation described in Robinet et al. (2020a, 2020b). An overview of the model is provided in Figure 2 and the reader is referred to the aforementioned papers for more details. LX-Shore simulates shoreline change resulting from the combination of cross-shore transport driven by changes in incident wave energy and gradients in total longshore sediment transport (Figure 2b). Based on earlier work (Ashton et al., 2001; Ashton and Murray, 2006) LX-Shore computes changes in the relative amount of dry (i.e. land) surface in square cells discretizing horizontally the computation domain. The spatial resolution of grid cells Δxy is typically in the range of 10–100 m. Dry cell fraction ranges from F = 0 (water cells) to F = 1 for fully dry sandy and/or rocky cells. Indeed, LX-Shore also includes non-erodible areas such as coastal defences and headlands with time-invariant rocky cell fraction (F_R) contribution : $F = F_S + F_R$, with F_S the sandy fraction. The shoreline is constructed using an interface reconstruction method, allowing the algorithm to handle complex shoreline geometries (e.g. sand spits, islands). Change in sediment fraction within the cells can result from longshore transport computed using the formula of Kamphuis (1991) and from cross-shore transport using an adaptation of the equilibrium-based ShoreFor model (Davidson et al., 2013; Splinter et al., 2014). The sediment fraction within computation cells and resulting shoreline are updated at each time step (Δt).

Critical to sediment transport and shoreline changes are the breaking wave conditions, which can be computed through the direct formula of Larson et al. (2010), which is typically used in LX-Shore on academic cases or for open beaches with alongshore-uniform offshore bathymetry (Robinet et al., 2018). Otherwise, breaking wave conditions are computed using the spectral wave model SWAN (Booij et al., 1999) to address configurations such as when complex wave shadowing or offshore wave transformation (e.g., energy focusing enforced by refraction, offshore wave energy dissipation through depth-induced breaking) affect breaking wave conditions and, in turn, sediment transport and shoreline change. At each time step LX-Shore provides an updated bathymetry that feeds back onto wave transformation. This updated bathymetry is reconstructed (Figure 2c) from the current shoreline position and the combination of two different idealized static equilibrium (Dean) beach profiles, for the sandy shores and for the rocky sectors.

2.2. *Simulation set-up and analysis*

LX-Shore was run for different embayed beach configurations schematised in Figure 3 with x and y the cross-shore and longshore coordinates, respectively. Embayed beaches were characterised by a length

W and headland length L, with the time-varying shoreline position denoted $S(y,t)$, with t the time. Periodic lateral boundary conditions were implemented so that headland sediment bypassing that occurs downdrift feeds the updrift part of the embayment. In other words, we assumed a circular system with constant sediment budget. This assumption will be discussed in Section 4. All simulations started from a uniform shoreline position S = 0. Twenty years of wave hindcast were used, defined by time series of significant wave height Hs, peak wave period Tp, and peak angle of incidence θ. A time-invariant directional spreading σ_θ of 40° was used, although additional simulations were run for other values of σ_θ (see Section 3.3). We used a wave hindcast (Durrant et al., 2014) offshore of Sydney (January 1, 1994 – January 1, 2014). Such wave climate is known to drive important rotation signal (Ranasinghe et al., 2004; Harley et al., 2015; Robinet et al., 2020a). Preliminary tests using W = 1000 m (comprising a total headland width of 200 m) and different headland lengths L indicated that model spin-up from the initial uniform shoreline typically lasted a few months. Therefore, the two first years of shoreline evolution were disregarded to insure that the simulated shoreline variability operates around a true dynamic equilibrium, and the subsequent 18 years (January 1, 1996 – January 1, 2014) were analysed.

Although cross-shore processes are found to affect embayment rotation, earlier work under the same wave climate as in Figure 3b (Robinet et al., 2020a) shows that cross-shore processes mainly drive a slightly alongshore variable cross-shore migration signal on the timescales from hours (storms) to months. In addition, the cross-shore transport module, which is based on ShoreFor (Davidson et al., 2013; Splinter et al., 2014), uses free parameters that depend on breaking wave conditions. Using a different headland length, results in different sheltering effects and, in turn, different breaking wave conditions that require a new calibration effort even under the same offshore wave climate. However, these calibration data do not exist for such academic cases. For all these reasons, cross-shore processes were switched off in all our simulations, which will be further discussed in Section 4.

Wave transformation was computed by SWAN model with default settings. Diffraction was not activated given that it shows poor skill unless fine grid resolution is used (Enet et al., 2006), and that LX-Shore shows very good skill on natural beaches without diffraction (Robinet et al., 2020a). LX-Shore simulations were run with grid cell size Δxy = 50 m and a constant time step Δt = 3 hours. SWAN cell size ("hydrodynamic grid") was 25 m. The water depth (h) was retrieved at each time step using an equilibrium Dean profile (Dean, 1991) on sandy sectors, given by $h = \alpha d^{\beta}$, with α and β two free model parameters. In the present study, we use values representative of Narrabeen beach (Robinet et al., 2020a), i.e. $\alpha = 0.25$ and $\beta = 0.67$. The profile was projected offshore from the current shoreline position where d is the distance offshore from the shoreline. The same applied for rocky shoreline with a steep profile also following a power law $h = ad^{b}$ with a = 1 and b = 1 chosen arbitrary (linear profile,

Figure 2c). When transects intersected, specific conditions including weighted averages were applied (for more detail see Robinet et al., 2018) to produce a consistent and smoothed bathymetry. In all simulations SWAN offshore boundary was located at x = 800 m in approximately 16-18 m depth. All simulations were performed for an embayment beach length W = 1000 m (comprising 200 m headland), although additional simulations were run for shorter and longer embayments (see Section 3.3). Headland length L was varied from 0 to 700 m, every 50 m, with additional simulations for L = 75 m, 125 m and 175 m to capture subtle changes in embayment shoreline response for this range of headland lengths.

Shoreline response was analysed using a set of variables (Figure 3), including the 18-year average (denoted $\bar{(\cdot)}$), hereafter referred to as mean, shoreline position $\bar{S}(y)$, its most eroded position $\bar{S}_{min}$ and corresponding longshore position $y(\bar{S}_{min})$, and the cross-shore standard deviation of shoreline position $\sigma_S(y)$. We also computed the mean shoreline rotation $\bar{R}$, which can also be referred to as orientation, as the slope of the trend-line fitted to $\bar{S}$. In order to address the spatial and temporal modes of shoreline variability, empirical orthogonal function (EOF) analysis of the shoreline deviation from the mean, i.e. $dS = S - \bar{S}$, was performed on the 18-year period. The analysis was performed at 150 m < y < 850 m to ignore the influence of spurious shoreline interpolation near the headlands. Finally, occurrence of headland sand bypassing was detected at each time step as $F_S > 0$ at the tip of the northern and/or southern headland(s). In order to address the wave control on embayed beach rotation we computed the power of the shore-parallel propagating wave component Pl, which is indicative of the portion of wave power available to drive alongshore currents in the surf zone (Price and Ruessink, 2011).

3. Results

3.1. *Mean embayed beach planform*

Figure 4 shows the mean shoreline $\bar{S}$ obtained for different headland lengths, together with the alongshore-uniform shoreline without headland (L = 0). Results show that mean shoreline planform varies from a reasonably straight rotated shoreline (e.g., L = 50 m), to a curved shoreline (e.g., L = 700 m), through an asymmetric and slightly curved shoreline with large erosion in the southern sector (e.g., L = 150 m). The mean embayed beach planforms also suggest headland sediment bypassing for certain headland lengths, e.g. for L = 50 m, for which the mean shoreline position at the northern end of the embayment coincides with the headland extremity.

Figure 5 provides more insight into the influence of headland length on mean embayed beach planform characteristics and how they relate to headland sand bypassing. Two categories of mean shoreline planforms can be discriminated, with a separation at headland length of $L \approx$ 150 m. For L < 150 m,

both shoreline orientation $\bar{R}$ and maximum erosion $|\bar{S}_{min}|$ rapidly increase with increasing headland length, with the opposite behaviour observed for L > 150 m (Figure 5a,b). Such a threshold is, however, not clearly observed for the alongshore location of maximum erosion $y(\bar{S}_{min})$, which becomes increasingly close to the centre of the embayment as headland length increases (Figure 5c). The change in mean shoreline behaviour corresponds to the transition between occasional headland sand bypassing and no headland sand bypassing (Figure 5d). For L = 150 m headland sediment bypassing only occurs $B = 0.2\%$ of the time, which contrasts with shorter headlands (e.g. B = 55.3% for L = 50 m and B = 23.7% for L = 100 m), while headland sediment bypassing never occurs (B = 0) for $L > 150$ m. Overall, when headland sediment bypassing never occurs, the mean shoreline planform becomes increasingly symmetric and curved, with a less severe shoreline retreat in the embayment, with increasing headland length (Figure 4b). At the same time, embayed beach orientation and prevailing angle of offshore wave incidence are increasingly different. In contrast, for $L < 150$ m as headland length is decreased allowing more frequent headland sediment bypassing, embayed beach planform becomes increasingly symmetric with its orientation increasingly deviating from the prevailing angle of wave incidence, while maximum erosion within the embayment at y ≈200 m is increased (Figure 4b).

3.2. *Modes of shoreline variability*

Figure 6 provides insight into the spatial and temporal evolution of the embayment shoreline for three representative simulations: i) short headlands with headland sand bypassing (L = 100 m, B = 23.7%, Figure 6c,d); ii) intermediate-length headlands with no headland sand bypassing (L = 250 m, Figure 6e,f) and iii) long headlands with no headland sand bypassing (L = 600 m, Figure 6g,h). In the case of frequent sand bypassing, the mean shoreline is curved, asymmetric, with a more rectilinear form in the northern section of the embayment. The pivot zone, i.e. where σ_S is minimized, is located at $y \approx$ 600 m, that is, not in the centre of the embayment. The shoreline variability reaches its maximum against the northern headland, where both σ_S and cross-shore amplitude are locally maximised at $y \approx$ 800 m, and is more homogeneous along the southern section (y < 550 m) of the embayment (Figure 6c,d). In contrast, in the case of intermediate-length headlands with no headland sand bypassing, the mean shoreline is still strongly asymmetric, but with a pivot zone closer to the centre of the embayment and with most of shoreline variability approximately equally distributed between the northern and southern sectors (Figure 6e). The cross-shore amplitude of shoreline position for intermediate-length headlands is also larger than for the situation with headland sand bypassing, with an amplitude exceeding 65 m near the embayment extremities (Figure 6e,f). In the case of a longer headland, still with no headland sand bypassing, both the mean embayed beach planform and

shoreline variance σ_S are essentially symmetric (Figure 6g). Shoreline variability is still maximized at the extremities of the embayment, with a maximum amplitude decreasing to 18 m (Figure 6h).

Figure 7 shows the first EOF mode for each of the same three simulations, providing additional insight into the spatial and temporal modes of shoreline variability for different headland lengths. It highlights a clear rotation response between the opposite ends of the embayment for both intermediate-length (L = 250 m) and long (L = 600 m) headlands, with a pivot zone at $y \approx$ 600 m and $y \approx$ 500 m, respectively. In each case, this rotation signal accounts for more than 95% of the total shoreline variability, with positive (negative) values of temporal mode $c_1(t)$ signifying a clockwise (counterclockwise) rotation of the embayed beach planform. The simulation with intermediate-length (L = 250 m) exhibits a first temporal mode essentially similar in pattern with the one obtained with the long (L = 600 m) headland, with a large interannual variability. The first EOF mode of the short headland simulation (L = 100 m) explains less variability (74.9%) and, contrary to the two previous examples, it does not correspond to a pure rotation mode as it is associated with a change in curvature (Figure 7a). This mode of shoreline variability indicates that when the shoreline tends to rotate clockwise (dominant northerly longshore transport), the shoreline also tends to be stable at the southern end of the embayment, which is expected to be the signature of headland sand bypassing feeding the southern sector of the embayment. Compared to simulations with longer headland for which there is no headland sand bypassing, the temporal EOF mode shows increased amplitude, particularly in higher frequency variability, although interannual variability is still present.

The difference in shoreline behaviour observed with no headland sand bypassing between intermediate-length (Figure 6e) and long (Figure 6g) headlands can be explained by the difference in wave shadowing patterns by the upwave headland and resulting different alongshore variability in breaking wave height conditions. This is illustrated in Figure 8 that shows the wave field for typical southeast swell conditions on May 16, 1995 (Hs = 1.2 m, Tp = 7.72, θ = 132.9°) for different headland length L = 250 m, 500 m and 600 m. Wave shadowing effects readily increase with increasing headland length (Figure 8). For intermediate-length headland L = 250 m (Figure 8a) the embayment shoreline varies from fully exposed to wave conditions in the northern sector to well sheltered at the southern end of the embayment, maximizing alongshore gradients in longshore sediment transport and resulting shoreline change (Figure 6e,f). For longer headlands, although wave shadowing and resulting alongshore variability in breaking wave height are large, the alongshore-averaged breaking wave height is largely reduced (Figure 8b,c), therefore limiting longshore transport gradients and resulting shoreline change (Figure 6g,h).

3.3. *Influence of directional spreading and embayed beach length*

Figure 9 shows that for a headland length L = 500 m (no headland sand bypassing) the mean embayed beach planform is much more curved and asymmetric for a time-invariant directional spreading σ_θ = 10° than for σ_θ = 40° (Figure 9a,d). Shoreline position also shows larger variance by a factor exceeding 3 (Figure 9c,f). Although the time-invariant directional spreading does not readily affect the temporal mode of rotation (Figure 9c,f), it affects the spatial mode as the rotation is associated with a slight change in overall shoreline curvature for σ_θ = 10° (Figure 9e). This can be explained by an inspection of the wave field for different directional spreadings. Figure 10 also that changes in directional wave spreading σ_θ have a profound impact on the wave shadowing zone and resulting alongshore variability in breaking wave height, with sharper gradients in breaking wave height for narrow-banded waves (Figure 10d). This is expected to favour changes in curvature.

Figure 11 shows the first temporal EOFs (rotation mode) for simulations with W = 500 m and W = 1000 m both for L = 200 m (no headland sand bypassing around the headland). Results show that the narrowest embayment respond at much shorter timescales (Figure 11b). Rotation signal for W = 1000 m correlates well with the 1-yr moving averaged $\tilde{P}_l$ (Figure 11a), while the smallest embayment seems to respond on the timescales of days, in response to changes in Pl. Other simulations (not shown) indicate that for longer embayments (W > 1000 m) the characteristic rotation timescale does not evolve much, instead it is the spatial mode that slowly evolves from a pure rotation pattern to rotation pattern associated with a change in shoreline curvature.

4. Discussion

Our simulations indicate that the onset of headland sediment bypassing is critical to both embayed beach equilibrium planform and the spatial and temporal modes of shoreline variability. These findings on the underrated role of headland sediment bypassing are in line with earlier observation on mean embayed beach planform (Goodwin et al., 2013). Our simulations show that, in addition, headland sand bypassing changes shoreline variability from a pure rotation mode to a more complex rotation mode where curvature is also modified. Embayed beaches where headland sand bypassing occurs also show more variability on short timescales. These results will need to be compared with a systematic assessment of embayed beach response timescales for a wider range of embayed beaches and headland lengths. Shoreline and embayed beach rotation monitoring techniques from freely-available satellite imagery (e.g., Vos et al., 2019) will be critical to address such embayed beach behaviour globally. Overall, hybrid shoreline models like LX-Shore (Robinet et al., 2018, 2020a), and others (e.g. Hurst et al., 2015), appear as relevant new tools to explore embayed beach shoreline dynamics, in

parallel to more empirical approaches (e.g., Gonzales and Medina, 2001; Klein et al., 2003a; Elshinnawy et al., 2018a) looking at equilibrium beach planshape.

Hurst et al. (2015) tested different spreads of schematic and monochromatic wave conditions and showed that embayed beach planform curvature decreases with the spread of wave directions. Here, we only used a single time series of realistic wave conditions. Clearly, the considered wave climate offshore of Narrabeen shows a narrowly peaked angular distribution (Figure 3b), which limits embayed beach shoreline dynamics. A greater variety of wave climates will need to be considered in future modelling experiments, ranging from low to high angles waves. It is expected that the alternation between near shore-normally incident waves, exerting a shoreline straightening influence, and highly-obliquely incident waves will lead to larger stochastic variations in local effective diffusivity (Ratliff and Murray, 2014). We also anticipate that it will lead to larger changes in beach curvature and enhanced breathing mode. The role of multi-modality of wave climate on rotation and breathing modes should also be investigated. Recent work (e.g. Wiggins et al., 2019a, 2019b) indicate that bimodal wave climate, which is common on many coasts (Scott et al., 2020), can lead to dramatic beach rotation events from the timescale of storm to decades. In such bimodal wave climate, the absence of shore-normal condition resulting in vanishing shoreline diffusivity may also allow for greater-amplitude fluctuations in shoreline curvature. To the best of our knowledge, the role of such wave climate bimodality on the spatial and temporal modes of shoreline variability has never been studied. Instead of addressing the directional spread in wave climate, we investigated the influence of the time-invariant directional spreading of each incident wave condition. Our results (Figure 9) show that the embayed beach planform is much more curved and asymmetric for narrow directional spreading, which is in line with Elshinnawy et al. (2018a) and consistent with the findings of Hurst et al. (2015). Shoreline position also shows larger variance for σ_θ = 10° than for σ_θ = 40°, and rotation signal is also associated with a change in overall curvature for a narrow directional spreading σ_θ = 10° (Figure 9e). This is consistent with the results of Ratliff and Murray (2014) who found an important breathing signal, reflecting a change in shoreline curvature, at idealised embayed beaches where monochromatic obliquely incident waves resulted in sharp shadowed-exposed wave energy gradients. However, at this stage we cannot explain why rotation and curvature change signals are not orthogonal EOF modes of shoreline behaviour in our simulations, contrary to simulations in Ratliff and Murray (2014) in which rotation and breathing modes were clearly discriminated. These results have strong implications, as they suggest that time series of parametric wave conditions (Hs, Tp, θ), which are typical products of global and regional wave hindcasts (e.g., Poli et al., 2016), are not enough to provide a fair description of both embayed beach equilibrium planform and rotation signal, and that directional spreading must also be accounted for.

Simulations were run to explore the role of W on embayed beach response. Model spin-up was found to dramatically increase with increasing W, with for instance an approximately 10-yr model spin-up for W = 2000 m (L = 300 m), compared to less than 2 years for W = 1000 m. Computation cost can therefore become prohibitive for large coastal embayments. Empirical equilibrium embayed beach profile approaches (e.g., Hsu et al., 2010), which are computationally cheap, should be preferred in such situations, bearing in mind they cannot address the time and spatial models of shoreline variability. Such long model spin-up is also in line with Hurst et al. (2015) who showed that the time taken for modelled bays to reach equilibrium scales with the square of the distance between headlands. This also corroborates the results of Ratliff and Murray (2014) who found a diffusing scaling, similar with the analytical findings of previous studies of e.g. Turki et al. (2013b), whereby increasing the alongshore length of embayed beach or decreasing the wave heights, will tend to result in nonlinear increases in the characteristic time scales. This emphasizes that, for a given headland length, small embayed beaches respond and recover from perturbations more rapidly than larger bays. Prohibitive model spin-up time for long embayments using our model set-up prevented from running a comprehensive analysis on this topic.

In addition to some model limitations detailed in Robinet et al. (2018), and in Robinet et al. (2020a) specifically for embayed beaches, here cross-shore processes were switched off. Robinet et al. (2020a) indicated that cross-shore processes primarily control the cross-shore, slightly alongshore non-uniform, translation mode of variability at Narrabeen-Collaroy embayment. However, different embayment widths, headland lengths and wave climate may have a profound impact on the relative contributions of cross-shore and longshore processes to rotation signal. In addition, other morphodynamic processes (see review of Loureiro and Ferreira, 2020) can affect embayment rotation, such as for instance shoreline-sandbar-coupled rotation driven by strong longshore components during storms (van de Lageweg et al., 2013), or high-energy rips flowing against the headland (Loureiro et al., 2012b). More shoreline modelling is required on real embayed beaches with different hydrodynamic and geological settings, in order to better constrain academic modelling experiments and gain generic knowledge of the processes driving rotation.

We found that headland sand bypassing is important to embayed beach behaviour. However, it must be pointed out that sediment bypass only occurs in our model when the sandy shoreline reaches the tip of the rocky headland, while it is well established that headland sediment bypassing can occur in the surf zone or even farther offshore through boundary rips (Castelle et al., 2016; Valiente et al., 2019; Sous et al., 2020). The degree of headland sand bypassing therefore strongly depends on the surf zone width relative to headland length (Klein et al., 2020). The critical headland length in the present study is likely underestimated and the 150 m value should be considered as low bound. Given that surf zone

width depends on beach profile characteristics defined by a Dean profile based on Narrabeen characteristics (Robinet et al., 2020a), changing such profile characteristics should also affect headland sand bypassing and, in turn, mean embayment planshape and shoreline dynamics. To tackle these issues, a more realistic contribution of headland sand bypassing (e.g. McCarroll et al., 2020) will need to be implemented in LX-Shore. We used synthetic headland shapes. However, headland geometry shows a striking natural variability (Fellowes et al., 2019 ; Figure 1), which deeply affects wave shadowing regions and accommodation space for sand deposit and, in turn, embayed beach shoreline behaviour. We used periodic lateral conditions, meaning that the amount of sediment leaving the domain in the north enters the domain from the south and vice versa. In reality, this perfectly circular system behaviour does not exist. Different rates of sediment supply/sink due to different lengths and shapes of the headlands likely impacts the mean embayed beach planform and modes of shoreline variability. This is however difficult to implement numerically as the amount of sediment entering the system depends on many updrift beach variables, including headland length, beach width and orientation, which also depend on the further updrift embayment, and so on. Therefore our work is complementary to previous ones which disregarded headland sand bypassing and assumed embayed beaches as closed systems (e.g. Hurst et al., 2015). Our results provide general trends in embayed beach behaviour but encourage application of such modelling approach to natural embayed beaches for more quantitative local assessment, such as in Robinet et al. (2020a) at Narrabeen-Collaroy embayment.

5. Conclusions

Our simulations show that headland length controls both the embayed beach equilibrium planform and the spatial and temporal modes of shoreline variability. For short headlands promoting occasional headland sand bypassing, embayed beach curvature increases with increasing headland length while the opposite is observed for headlands long enough to prevent any headland sand bypassing occurrence. The onset of headland sand bypassing also controls embayed beach rotation signal. When there is no sand bypassing, rotation signal decreases in amplitude, resulting in less shoreline variance, and becomes increasingly symmetric with increasing headland length. The modal directional spreading of incident waves is also critical to embayed beach behaviour, with both shoreline embayment curvature and shoreline variance increasing with decreasing modal directional spreading. Embayed beach rotation characteristic timescale increases with increasing embayed beach length, while shoreline variance decreases across the entire embayment. Our simulations provide new insight into the influence of embayed beach characteristics and incident wave conditions on equilibrium planform and shoreline dynamics, implying that the potential occurrence of headland sand bypassing should be considered in future embayed beach classifications. State-of-the-art models coupling spectral wave

and shoreline change modules such as LX-Shore (Robinet et al., 2018) appear as a powerful tool to describe and further predict embayed beach behaviour, and to design coastal structures (e.g. groins, jetties), in parallel to the continuous development of empirical embayed beach planform models (e.g., Hsu et al., 2010).

Acknowledgments

BC funded by Agence Nationale de la Recherche (ANR) grant number ANR-17-CE01-0014; MD PhD scholarship funded by BRGM and Make Our Planet Great Again (MOPGA) national program. DI and AR funded by BRGM. We thank M.D. Harley and K.D. Splinter from Water Research Laboratory (UNSW) team for sharing the Sydney wave data kindly provided by the Manly Hydraulics Laboratory on behalf of the NSW OEH.

References cited

Antolínez, J.A.A., Méndez, F.J., Anderson, D., Ruggiero, P., Kaminsky, G.M., 2019. Predicting climate driven coastlines with a simple and efficient multi-scale model. Journal of Geophysical Research Earth Surface, 124, doi:10.1029/2018JF004790.

Ashton, A.D., Murray, A.B., 2006. High-angle wave instability and emergent shoreline shapes: 1. Modeling of sand waves, flying spits, and capes. Journal of Geophysical Research, 111, doi: 10.1029/2005JF000422.

Ashton, A.D., Murray, A.B., Arnoult, O., 2001. Formation of coastline features by large-scale instabilities induced by high-angle waves, Nature, 414, 296–300. doi:10.1038/35104541.

Blossier, B., Bryan, K.R., Daly, C.J., Winter, C., 2016. Nearshore sandbar rotation at single-barred embayed beaches, Journal of Geophysical Research Oceans, 121, 2286–2313, doi:10.1002/2015JC011031.

Booij, N., Ris, R.C., Holthuijsen, L.H., 1999. A third-generation wave model for coastal regions: 1. Model description and validation. J. Geophys. Res. Oceans 104, 7649–7666, doi: 10.1029/98JC02622.

Castelle, B., Coco, G., 2012. The morphodynamics of rip channels on embayed beaches. Continental Shelf Research, 43, 10–23.

Castelle, B., Scott, T., Brander, R.W., McCarroll, R.J., 2016. Rip current types, circulation and hazard. Earth-Science Reviews, 163, 1–21

CEREMA, 2017. Cartographie nationale des ouvrages et aménagements littoraux, In French, http://www.geolittoral.developpement-durable.gouv.fr/cartographie-nationale-des-ouvrages-et-r502.html.

461 Daly, C.J., Bryan, K.R., Winter, C., 2014a. Wave energy distribution and morphological development in
462 and around the shadow zone of an embayed beach. Coastal Engineering, 93, 40–54,
463 doi:10.1016/j.coastaleng.2014.08.003.
464 Daly, C.J., Bryan, K.R., Gonzalez, M.R., Klein, A.H.F., Winter, C., 2014b. Effect of selection and
465 sequencing of representative wave conditions on process-based predictions of equilibrium
466 embayed beach morphology. Ocean Dynamics, 64, 863-877.
467 Davidson, M.A., Splinter, K.D., Turner, I.L., 2013. A simple equilibrium model for predicting shoreline
468 change. Coastal Engineering, 73, 191–202.
469 Dean, R.G., 1991. Equilibrium beach profiles: characteristics and applications. Journal of Coastal
470 Research, 7, 53–84.
471 Durrant, T., Greenslade, D., Hemer, M., Trenham, C., 2014. A global wave hindcast focussed on the
472 Central and South Pacific. In: CAWCR Technical Report No. 70,
473 http://www.cawcr.gov.au/technical-reports/CTR_070.pdf.
474 Elshinnawy, A.I., Medina, R., Gonzalez, M., 2018a. On the influence of wave directional spreading on
475 the equilibrium planform of embayed beaches. Coastal Engineering, 133, 59-75.
476 Elshinnawy, A.I., Medina, R., Gonzalez, M., 2018b. Dynamic equilibrium planform of embayed beaches:
477 Part 1. A new model and its verification. Coastal Engineering, 135, 112-122.
478 Elshinnawy, A.I., Medina, R., Gonzalez, M., 2018c. Dynamic equilibrium planform of embayed beaches:
479 Part 2. Design procedure and engineering applications. Coastal Engineering, 135, 123-137.
480 Enet, F., Nahon, A., Van Vledder, G., Hurdle, D., 2006. Evaluation of diffraction behind a semi-infinite
481 breakwater in the SWAN wave Model. Proceedings, 9th International Workshop on Wave
482 Hindcasting and Forecasting (Victoria, BC, Canada).
483 Fellowes, T.E., vila-Concejo, A., Gallop, S.L., 2019. Morphometric classification of swell-dominated
484 embayed beaches. Marine Geology, 411, 78-87.
485 Gonzalez, M., Medina, R., 2001. On the application of static equilibrium bay formations to natural and
486 man-made beaches. Coastal Engineering, 43 (3–4), 209–225.
487 Goodwin, I.D., Freeman, R., Blackmore, K., 2013. An insight into headland sand bypassing and wave
488 climate variability from shoreface bathymetric change at Byron Bay, New South Wales,
489 Australia. Marine Geology, 341, 29–45, doi:10.1016/j.margeo.2013.05.005.
490 Hanson, H., 1989. Genesis - a generalized shoreline change numerical model. Journal of Coastal
491 Research, 5, 1–27.
492 Harley, M.D., Turner, I.L., Short, A.D., Ranasinghe, R., 2011. A reevaluation of coastal embayment
493 rotation: the dominance of cross-shore versus alongshore sediment transport processes,
494 Collaroy-Narrabeen Beach, southeast Australia. Journal of Geophysical Research, 116, F04033,
495 doi:10.1029/2011JF001989.

496 Harley, M.D., Andriolo, U., Armaroli, C., Ciavola, P., 2013. Shoreline rotation and response to
497 nourishment of a gravel embayed beach using a low-cost video monitoring technique: San
498 Michele-Sassi Neri, central Italy. Journal of Coastal Conservation, 18, 551–565, doi:
499 10.1007/s11852-013-0292-x.
500 Harley, M.D., Turner, I.J., Short, A.D., 2015. New insights into embayed beach rotation: the importance
501 of wave exposure and cross-shore processes. Journal of Geophysical Research Earth Surface,
502 120, 1470–1484, doi: 10.1002/2014JF003390.
503 Hsu, J.R.C., Evans, C., 1989. Parabolic bay shapes and applications. Proceedings Institution Civil
504 Engineers Part 2 87, 557–570.
505 Hsu, J.R.C., Klein, A.H.F., Benedet, L., 2004. Geomorphic approach for mitigation beach erosion
506 downdrift of littoral barrier. Proceedings 29th International Conference Coastal Engineering:
507 ASCE, vol. 2, pp. 2022–2034.
508 Hsu, J.R.C., Yu, M.-J., Lee, F.-C., Benedet, L., 2010. Static bay beach concept for scientists and engineers:
509 a review. Coastal Engineering 57, 76–91.
510 Hurst, M.D., Barkwith, A., Ellis, M.A., Thomas, C.W., Murray, A.B., 2015. Exploring the sensitivities of
511 crenulate bay shorelines to wave climates using a new vector-based one-line model. Journal
512 of Geophysical Research Earth Surface, 120, 2586–2608, doi:10.1002/2015JF003704.
513 Jackson, D.W.T., Cooper, J.A., 2010. Application of the equilibrium planform concept to natural
514 beaches in Northern Ireland. Costal Engineering, 57, 112-123.
515 Kamphuis, J.W., 1991. Alongshore sediment transport rate. Journal of Waterway, Port, Coastal, and
516 Ocean Engineering, 117, 624–640, doi: 10.1061/(ASCE)0733-950X(1991)117:6(624).
517 Klein, A.H.F., Benedet, L., Schumacher, D.H., 2002. Short-term beach rotation processes in distinct
518 headland bay beach systems. Journal of Coastal Research, 18 (3), 442–458.
519 Klein, A.H.F., Benedet, L., Hsu, J.R.C., 2003a. Stability of headland-bay beaches in Santa Catarina: a case
520 study. Journal of Coastal Research SI 35, 151–166.
521 Klein, A.H.F., Vargas, A., Raabe, A.L.A., Hsu, J.R.C., 2003b. Visual assessment of bayed beach stability
522 using computer software. Computers and Geosciences 29, 1249–1257.
523 Klein, A.H.F., Vieira da Silva, G., Taborda, R., da Silva, A.P., Short, A.D., 2020. Headland bypassing and
524 overpassing: form, processes and applications. In: Sandy Beach Morphodynamics, Ed. D.
525 Jackson & A.D. Short, Elsevier, 557-591
526 Larson, M., Kraus, N.C., Hanson, H., 2002. Simulation of regional longshore sediment transport and
527 coastal evolution - the Cascade model. In: Proc. 28th Coastal Engineering Conference, World
528 Sci. Press.

529 Larson, M., Hoan, L.X., Hanson, H., 2010. Direct formula to compute wave height and angle at incipient
530 breaking. Journal of Waterway, Port, Coastal and Ocean Engineering, 136, 119–122, doi:
531 10.1061/(ASCE)WW.1943-5460.0000030.
532 Loureiro, C., Ferreira, O., Cooper, J.A.G., 2012a. Geologically constrained morphological variability and
533 boundary effects on embayed beaches. Marine Geology, 329–331, 1–15,
534 doi:10.1016/j.margeo.2012.09.010.
535 Loureiro, C., Ferreira, O., Cooper, J.A.G., 2012b. Extreme erosion on high-energy embayed beaches:
536 influence of megarips and storm grouping. Geomorphology 139-140, 155–171.
537 Loureiro, C., Ferreira, O., 2020. Mechanisms and timescales of beach rotation. In: Sandy Beach
538 Morphodynamics, Ed. D. Jackson & A.D. Short, Elsevier, 593-614
539 Martins, C., de Mahiques, M., 2006. Small scale beach rotation process on a reflective beach. Journal
540 of Coastal Research, 1, 542–546.
541 Masselink, G., Pattiaratchi, C.B., 2001. Seasonal changes in beach morphology along the sheltered
542 coastline of Perth, Western Australia. Mar. Geol. 172 (3–4), 243–263, soi:10.1016/S0025-
543 3227(00)00128-6.
544 McCarroll, R.J., Brander, R.W., Turner, I.L., Van Leeuwen, B., 2016. Shoreface storm morphodynamics
545 and mega-rip evolution at an embayed beach: Bondi Beach, NSW, Australia. Continental Shelf
546 Research, 11615 March 2016Pages 74-88.
547 McCarroll, R.J., Masselink, G., Valiente, N.G., King, E.V., Scott, T., Stokes, C., Wiggins, M., 2020. A
548 general expression for wave-induced sediment bypassing of an isolated headland.
549 https://doi.org/10.31223/osf.io/67rhx
550 Montaño, J., Coco, G., Antolínez, J.A.A., Beuzen, T., Bryan, K.R., Cagigal, L., Castelle, B., Davidson, M.A.,
551 Goldstein, E.B., Ibaceta, R., Idier, D., Ludka, B.C., Masoud-Ansari, S., Mendez, F.J., Murray, A.B.,
552 Plant, N.G., Ratliff, K.M., Robinet, A., Rueda, A., Sénéchal, N., Simmons, J.A., Splinter, K.D.,
553 Stephens, S., Townend, I., Vitousek, S., Vos, K., 2020. Blind testing of shoreline evolution
554 models. Sci. Rep. 10: 2137, doi:10.1038/s41598-020-59018-y.
555 Ojeda, E., Guillen, J., 2008. Shoreline dynamics and beach rotation of artificial embayed beaches.
556 Marine Geology, 253, 51–62, doi:10.1016/j.margeo.2008.03.010.
557 Poli, P., Hersbach, H., Dee, D.P., Berrisford, P., Simmons, A.J., Vitart, F., et al. (2016). Era-20C: An
558 atmospheric reanalysis of the twentieth century. Journal of Climate, 29(11), 4083–4097,
559 doi:10.1175/JCLI-D-15-0556.1.
560 Price, T.D., Ruessink, B.G., 2011. State dynamics of a double sandbar system. Continental Shelf
561 Research, 31 (6), 659–674, doi: 10.1016/j.csr.2010.12.018

562 Ranasinghe, R., McLoughlin, R., Short, A., Symonds, G., 2004. The Southern Oscillation Index, wave
563 climate, and beach rotation. Marine Geology, 204, 273–287, doi: 10.1016/S0025-
564 3227(04)00002-7.
565 Ratliff, K.M., Murray, A.B., 2014. Modes and emergent time scales of embayed beach dynamics,
566 Geophysical Research Letters, 41, 7270–7275, doi:10.1002/2014GL061680.
567 Rea, C., Komar, P.D., 1975. Computer simulation models of a hooked beach shoreline configuration,
568 Journal of Sedimentology Petrology, 45(4), 866–872.
569 Robinet, A., Idier, D., Castelle, B., Marieu, V., 2018. A reduced-complexity shoreline change model
570 combining longshore and cross-shore processes: The LX-Shore model. Environmental
571 Modelling and Software, 109: 1–16, doi: 10.1016/j.envsoft.2018.08.010.
572 Robinet, A., Castelle, B., Idier, D., Harley, M.D., Splinter, K.D., 2020a. Controls of local geology and
573 cross-shore/longshore processes on embayed beach shoreline variability. Marine Geology,
574 422, doi: 10.1016/j.margeo.2020.106118.
575 Robinet, A., D'Anna, M., Idier, D., Castelle, B., Le Cozannet, G., 2020b. Simulating the impact of sea-
576 level rise and offshore bathymetry on embayment shoreline changes. In: Malvárez, G. and
577 Navas, F. (eds.), Proceedings from the International Coastal Symposium (ICS) 2020 (Seville,
578 Spain). Journal of Coastal Research, Special Issue No. 95., 1263–1267.
579 Scott, T., Masselink, G., McCarroll, R.J., Castelle, B., Dodet, G., Saulter, A, Scaife, A.A., Dunstone, N.,
580 2020. Atmospheric controls and long range predictability of directional waves in the United
581 Kingdom & Ireland. Doi:10.1002/essoar.10503076.1
582 Short, A.D., Masselink, G., 1999. Embayed and structurally controlled embayed beaches, in: Short, A.D.,
583 (Eds.), 1999. Handbook of Beach and Shoreface Morphodynamics. Wiley, Chichester, pp. 230–
584 250.
585 Short, A.D., Trembanis, A.C., 2004. Decadal scale patterns in beach oscillation and rotation Narrabeen
586 beach, Australia—time series, PCA and wavelet analysis. Journal of Coastal Research, 20(2),
587 523–532.
588 Silvester, R., 1970. Growth of crenulate shaped bays to equilibrium. Journal of Waterway Harbors
589 Coastal Engineering Division, 96(2), 275–287.
590 Sous, D., Castelle, B., Mouragues, A., Bonneton, P., 2020. Field Measurements of a High-Energy
591 Headland Deflection Rip Current: Tidal Modulation, Very Low Frequency Pulsation and Vertical
592 Structure. J. Mar. Sci. Eng., 8, 534.
593 Splinter, K. D., J. T. Carley, A. Golshani, and R. Tomlinson (2014), A relationship to describe the
594 cumulative impact of storm

595 Splinter, K.D., Turner, I.L., Davidson, M.A., Barnard, P., Castelle, B., Oltman-Shay, J., 2014. A generalized
596 equilibrium model for predicting daily to interannual shoreline response. Journal of
597 Geophysical Research - Earth Surface, 119, 1936–1958, doi:10.1002/2014JF003106.
598 Szmytkiewicz, M., Biegowski, J., Kaczmarek, L.M., Okrój, T., Ostrowski, R., Pruszak, Z., Różyńsky, G.,
599 Skaja, M., 2000. Coastline changes nearby harbour structures: comparative analysis of one-line
600 models versus field data. Coast Eng. 40, 119–139, doi:doi.org/10.1016/S0378-3839(00)00008-
601 9.
602 Thomas, T., Phillips, M.R., Williams, A.T., 2010. Mesoscale evolution of a headland bay: beach rotation
603 process. Geomorphology 123, 129–141, doi:10.1016/j.geomorph.2010.06.018.
604 Tran, Y.H., Barthélemy, E., 2020. Combined longshore and cross-shore shoreline model for closed
605 embayed beaches. Coastal Engineering, doi:10.1016/j.coastaleng.2020.103692.
606 Turki, I., Medina, R., Gonzalez, M., Coco, G., 2013a. Natural variability of shoreline position:
607 Observations at three pocket beaches. Marine Geology, 338, 76–89,
608 doi:10.1016/j.margeo.2012.10.007.
609 Turki, I., Medina, R., Coco, G., Gonzalez, M., 2013b. An equilibrium model to predict shoreline rotation
610 of pocket beaches. Marine Geology, 346, 220–232, doi:10.1016/j.margeo.2013.08.002.
611 Valiente, N.G., Masselink, G., Scott, T., Conley D., McCarroll, R.J., 2019. Role of waves and tides on
612 depth of closure and potential for headland bypassing. Marine Geology, 407, 60–75,
613 doi:10.1016/j.margeo.2018.10.009.
614 Van de Lageweg, W.I., Bryan, K.R., Coco, G., Ruessink, B.G., 2013. Observations of shoreline–sandbar
615 coupling on an embayed beach. Marine Geology, 344, 101–114,
616 doi:10.1016/j.margeo.2013.07.018.
617 Vitousek, S., Barnard, P.L., Limber, P., Erikson, L., Cole, B., 2017. A model integrating longshore and
618 cross-shore processes for predicting long-term shoreline response to climate change. Journal
619 of Geophysical Research Earth Surface, 122 (4), 782–806, doi:10.1002/2016JF004065.
620 Vos, K., Harley, M.D., Splinter, K.D., Simmons, J.A., Turner, I.L., 2019. Sub-annual to multi-decadal
621 shoreline variability from publicly available satellite imagery. Coastal Engineering, 150, 160–
622 174.
623 Wiggins, M., Scott, T., Masselink, G., Russell, P., McCarroll, R.J., 2019a. Coastal embayment rotation:
624 Response to extreme events and climate control, using full embayment surveys.
625 Geomorphology, 327, 385-403, doi:10.1016/j.geomorph.2018.11.014.
626 Wiggins, M., Scott, T., Masselink, G., Russell, P., Valiente, N.G., 2019b. Regionally-Coherent
627 Embayment Rotation: Behavioural Response to Bi-Directional Waves and Atmospheric Forcing.
628 J. Mar. Sci. Eng., 7, 116.
629 Yasso, W., 1965. Plan geometry of headland bay beaches. Journal of Geology, 73, 702–714.

630 Yates, M.L., Guza, R.T., O'Reilly, W.C., 2009. Equilibrium shoreline response: observations and
631 modelling. Journal of Geophysical Research, 114, C09014, doi:10.1029/2009JC005359.
632

633 **Figures**

634

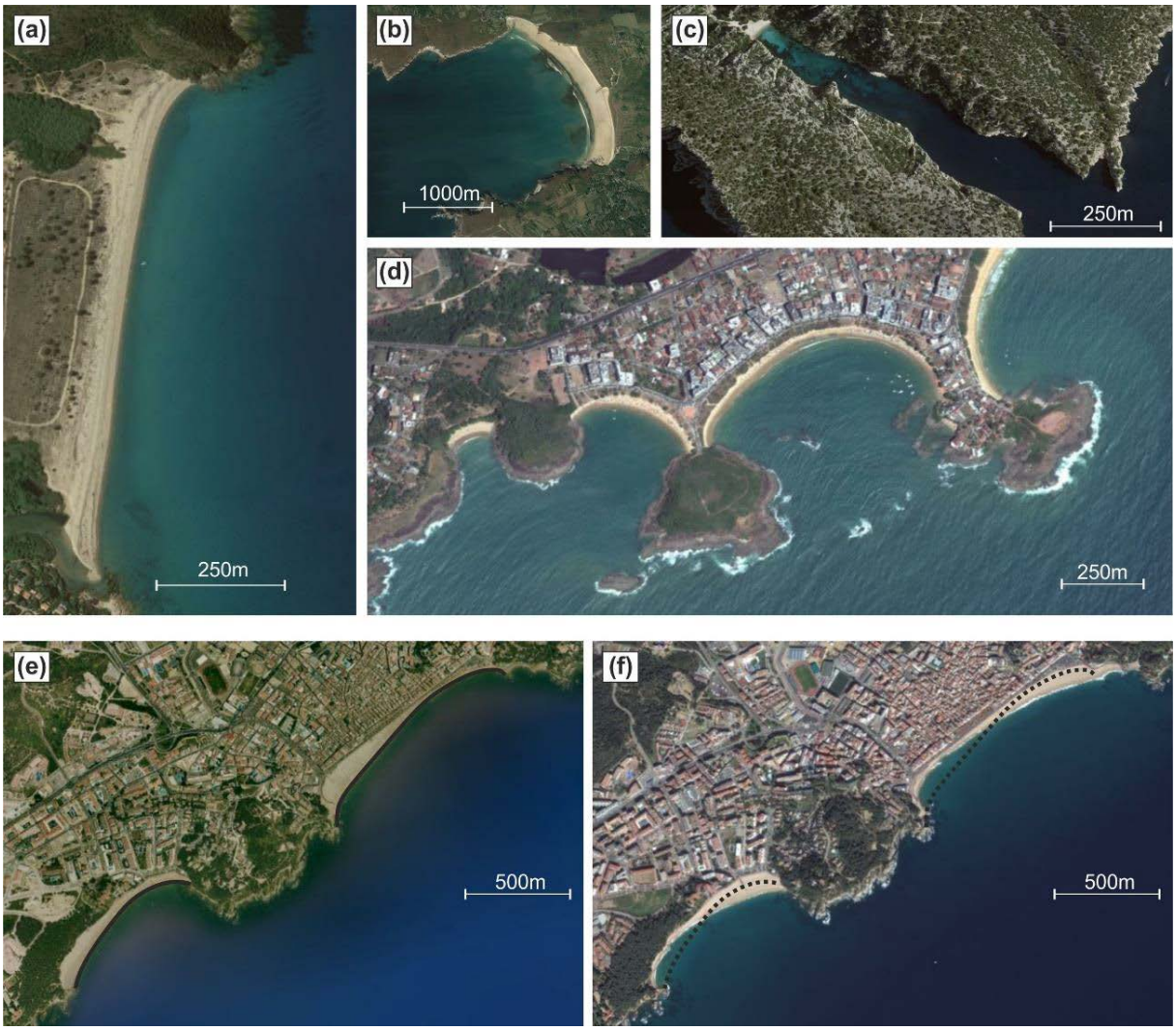

635

636 Figure 1. (a-d) Examples of typical embayed beach planforms from a relatively straight shoreline with
637 (a) low and (c) high indentation at Porto Vecchio (Corsica) and Cassis (southeast France), respectively,
638 to curved embayments at (b) Crozon (Brittany, northwest France) and (d) Guarapari (southeast Brazil).
639 (e,f) Illustration of dramatic variability in shoreline orientation resulting from embayment rotation at
640 Lloret de Mar (northeast Spain) (e) on June 2004 and (f) on March 2014 with in (f) the dotted the
641 shoreline position in (e). Images adapted from Google Earth.

642

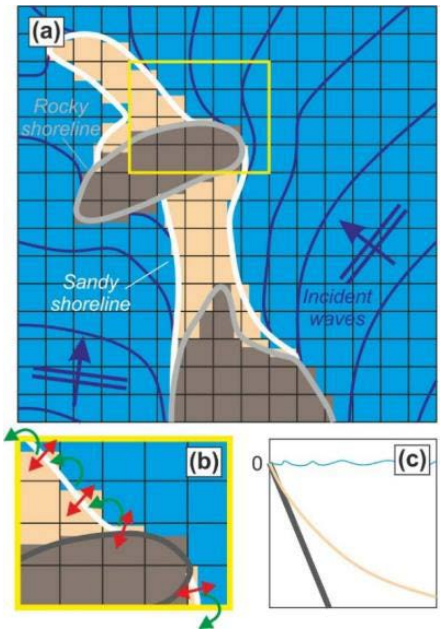

643

644 Figure 2. Overview of features and processes included in LX-Shore (adapted from Robinet et al., 2018,
645 2020a) with (a) schematic planview coastal area with non-erodible rocky areas, sandy shores and
646 incident waves; (b) zoom onto a sandy/rocky area showing where the longshore and cross-shore
647 sediment transports are computed; (c) idealised rocky (grey) and sandy (sand) profiles used to design
648 the updated nearshore bathymetry feeding back spectral wave model SWAN at each time step.

649

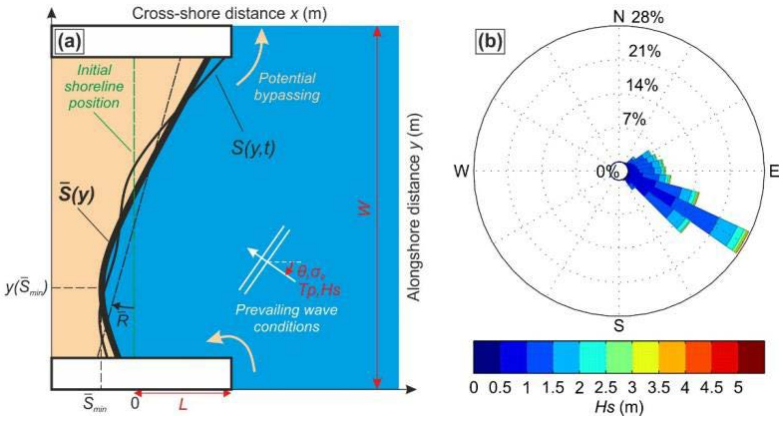

650

651 Figure 3. (a) Schematic of embayed beach model set-up with primary input and output variables used
652 for analysis and (b) significant wave height Hs rose of wave conditions used as offshore boundary
653 conditions. All variables in (a) are explained in the text.

654 Figure 4. (a) Mean shoreline planform obtained for different headland lengths L (coloured) with (b)
655 zoom to emphasize variability.

Figure 5. Mean embayed beach planform variables against headland length L: (a) rotation $\bar{R}$; (b) most eroded shoreline position $\bar{S}_{min}$; (c) corresponding alongshore location $y(\bar{S}_{min})$ and (d) percentage of occurrence of sediment bypass around the headland B.

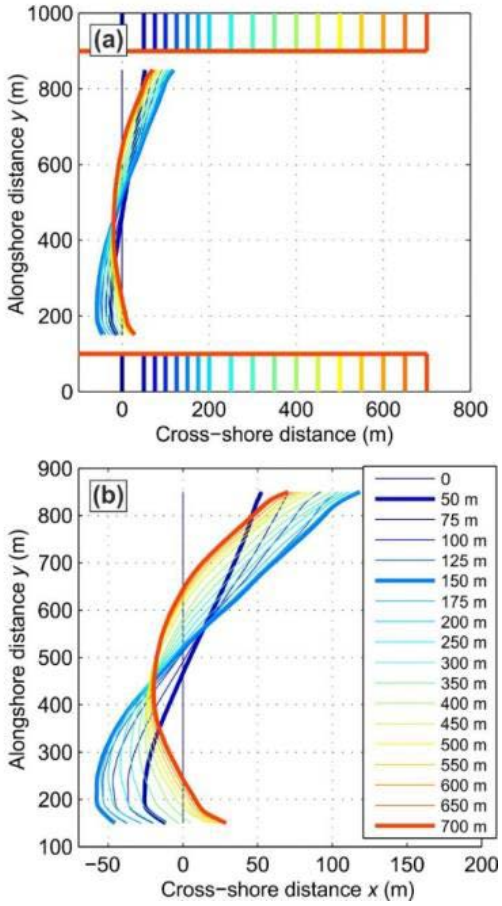

Figure 6. Time series of (a) significant wave height Hs and (b) alongshore component of offshore wave power Pl. Left-hand panels (c,e,g): mean (black line), cross-shore standard deviation σ_S (grey line) and envelope (yellow area) of simulated shorelines; Right-hand panels (d,f,h): time evolution of shoreline deviation from the mean dS for different headland lengths (c,d) L = 100 m; (e,f) L = 250 m; (g,h) L = 600 m.

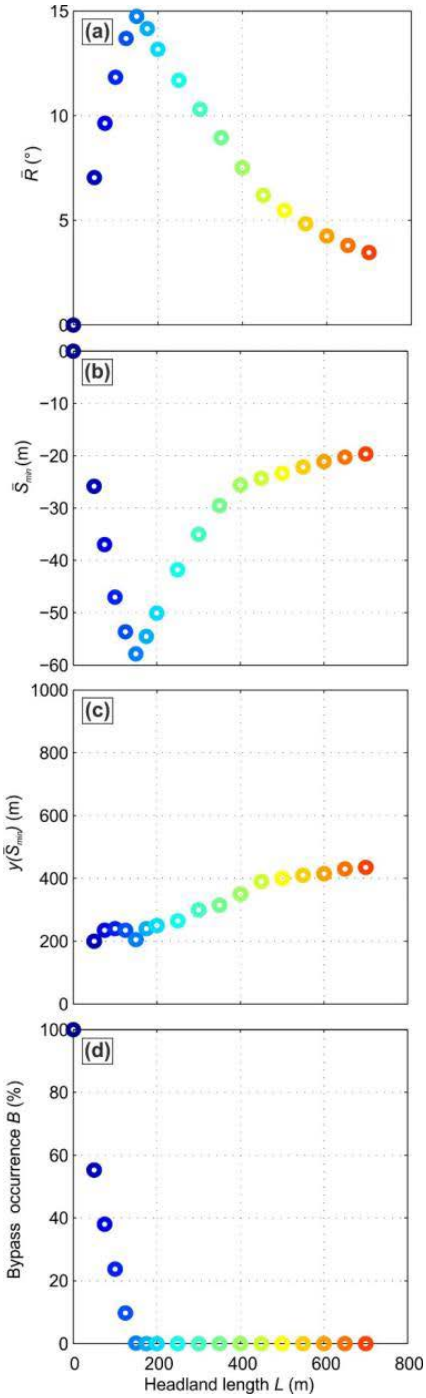

667

668 Figure 7. EOF analyses of dS showing the first (a) spatial and (b) temporal EOFs for simulations with L

669 = 100 m (green), L = 250 m (blue) and L = 600 m (red).

670

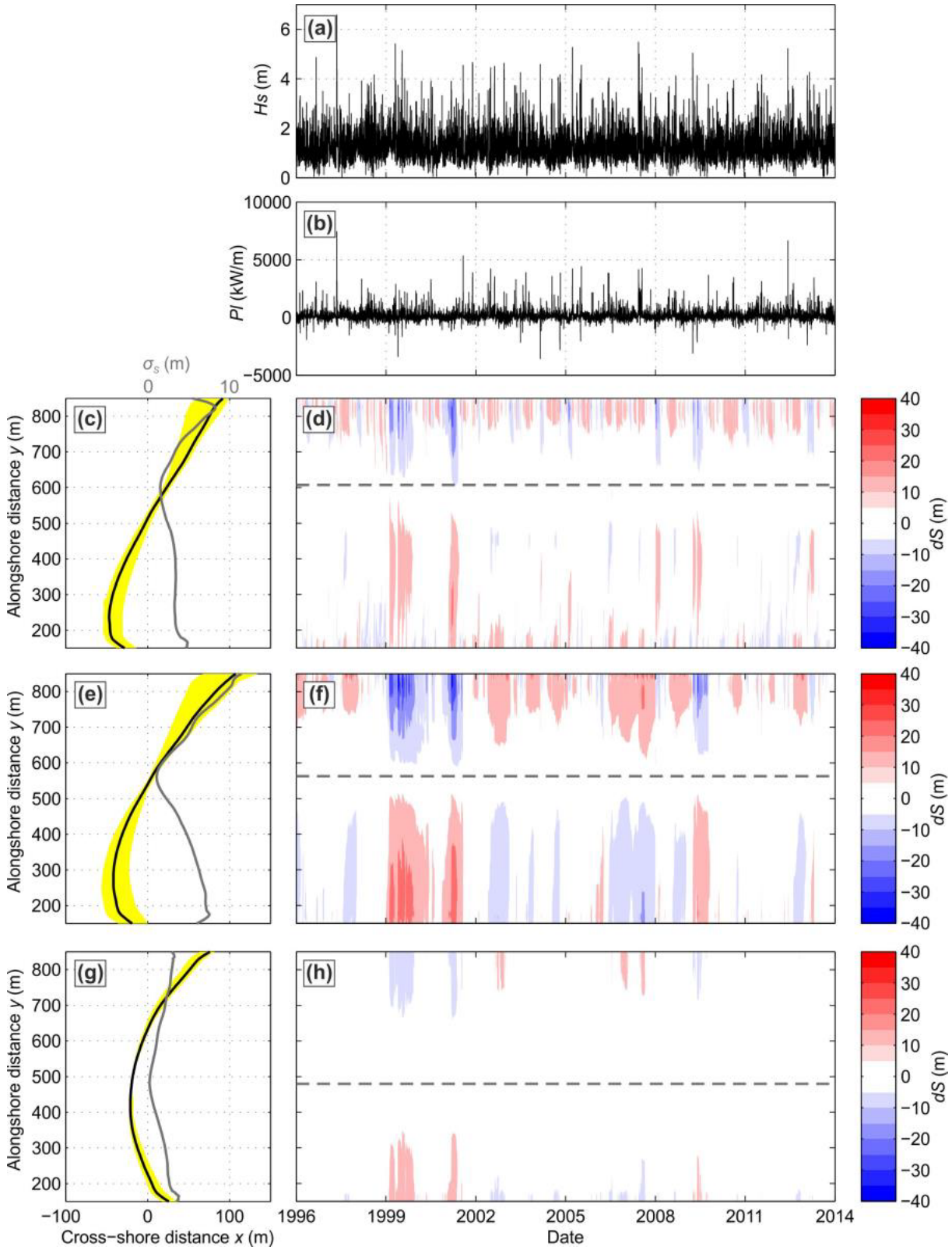

Figure 8. Significant wave height Hs field coloured on May 16, 1995 (Hs = 1.2 m, Tp = 7.72, θ = 132.9°) for different headland length (a) L = 250 m; (b) L = 500 m; (c) L = 600 m. In all panels, bathymetry is contoured in the background (black lines) at 2-m interval, with the thick grey line showing the embayment shoreline.

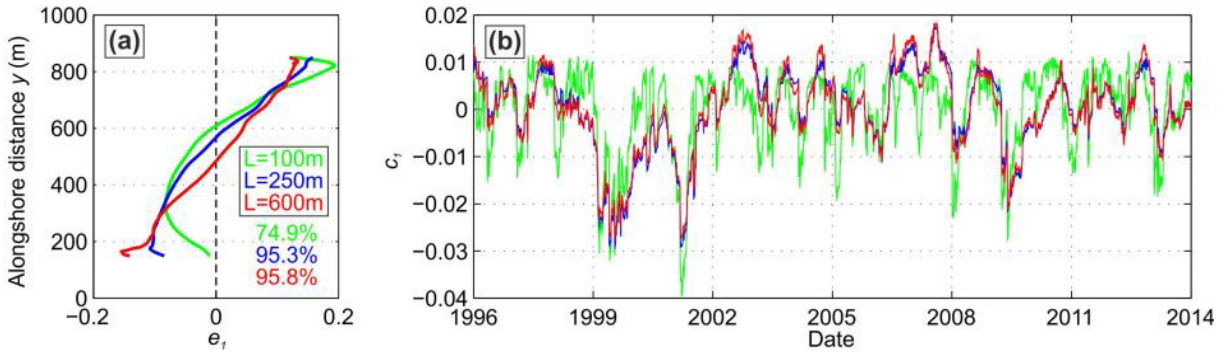

676

677 Figure 9. Left-hand panels: shoreline envelope (yellow area), mean shoreline planform (black line) and
678 cross-shore standard deviation σ_S (blue line); Middle panels: spatial component of the first EOF of ;
679 Right-hand panels: time evolution of shoreline deviation from the mean dS for L = 500 m for different
680 wave directional spreading (a-c) σ_θ = 40° and (d-f) $\sigma_\theta = 10°$.

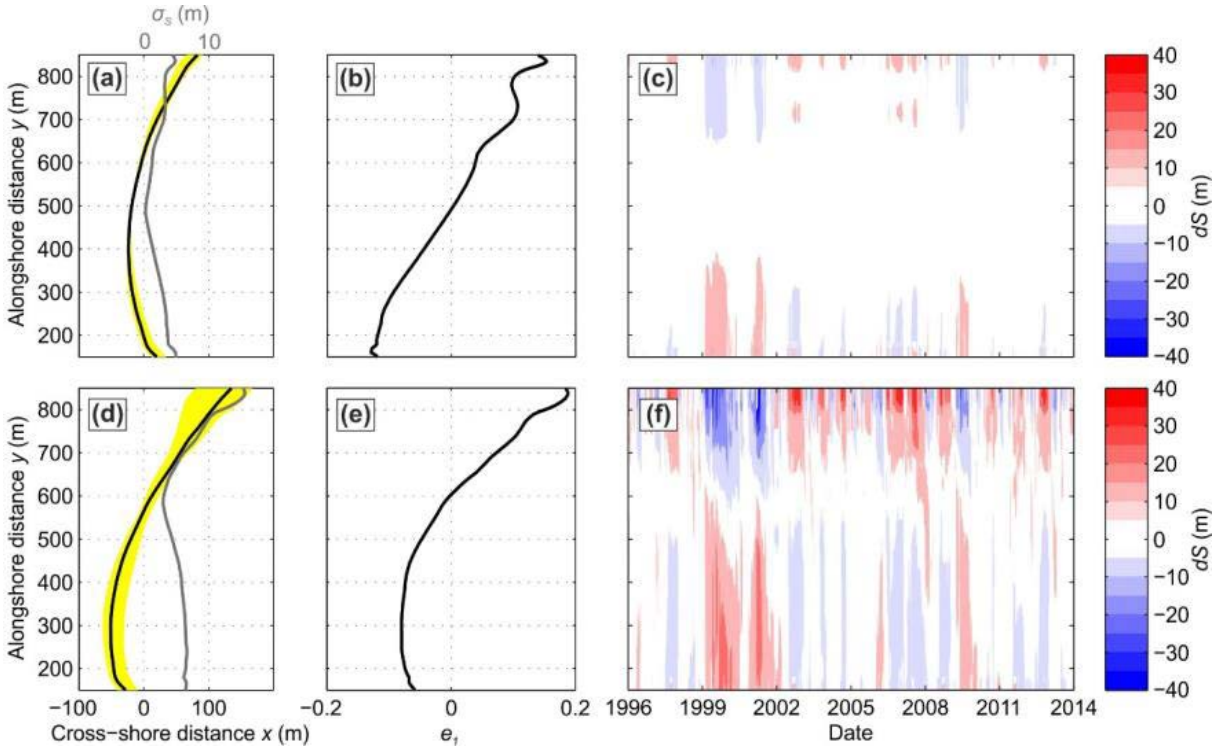

681

682

683 Figure 10. Embayed beach morphology and wave field (significant wave height Hs coloured) on
684 December 26, 1995 for different time-invariant directional spreading values (a) σ_θ = 40°; (b) σ_θ = 30°;
685 (c) σ_θ = 20°; (d) σ_θ = 10°.

686

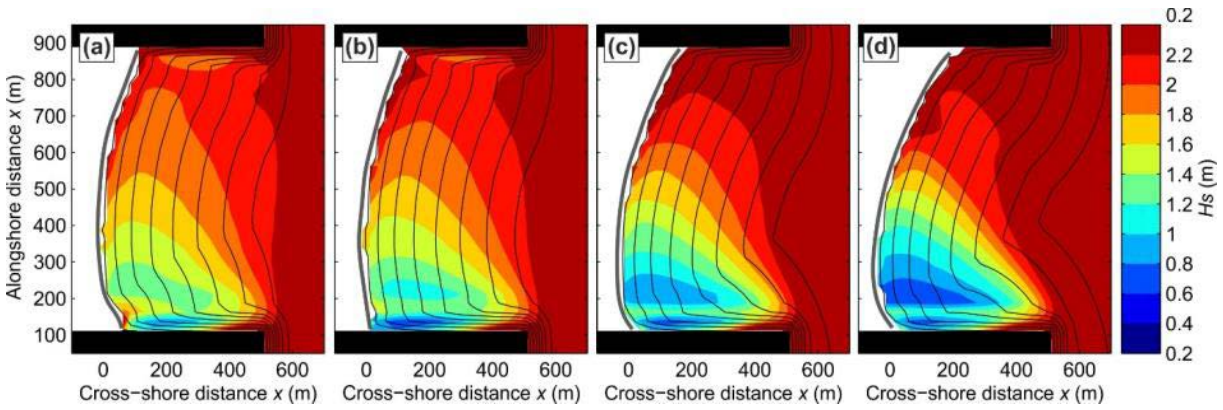

687

688 Figure 11. (a) Time series of alongshore component of offshore wave power Pl (black) and its 1-yr
689 moving average $\tilde{P}l$ (red); (b) first temporal EOFs of dS for simulations with W = 500 m (red) and W =
690 1000 m (blue) both for L = 200 m (no headland sand bypassing).